Multimodal Characterization of the Human Nucleus Accumbens

Samuel CD Cartmell, BA[1], **Qiyuan Tian, PhD**[2,3], **Brandon J Thio, BS**[4], **Christoph Leuze, PhD**[2], **Li Ye, PhD**[5], **Nolan R Williams, MD**[6], **Grant Yang, MS**[2,3], **Gabriel Ben-Dor, BS**[6], **Karl Deisseroth, MD PhD**[5,6], **Warren M Grill, PhD**[4], **Jennifer A McNab, PhD**[2], **Casey H Halpern, MD**[1]

[1]Department of Neurosurgery, Stanford University, Stanford, CA, 94305 USA

[2]Department of Radiology, Stanford University, Stanford, CA, 94305 USA

[3]Department of Electrical Engineering, Stanford University, Stanford, CA, 94305 USA

[4]Department of Biomedical Engineering, Duke University, Stanford University, Stanford, CA, 94305 USA

[5]Department of Bioengineering, Stanford University, Stanford, CA, 94305 USA

[6]Department of Psychiatry, Stanford University, Stanford, CA, 94305 USA

Abstract

Dysregulation of the nucleus accumbens (NAc) is implicated in numerous neuropsychiatric disorders. Treatments targeting this area directly (e.g. deep brain stimulation) demonstrate variable efficacy, perhaps owing to non-specific targeting of a functionally heterogeneous nucleus. Here we provide support for this notion, first observing disparate behavioral effects in response to direct simulation of different locations within the NAc in a human patient. These observations motivate a segmentation of the NAc into subregions, which we produce from a diffusion-tractography based analysis of 245 young, unrelated healthy subjects. We further explore the mechanism of these stimulation-induced behavioral responses by identifying the most probable subset of axons activated using a patient-specific computational model. We validate our diffusion-based segmentation using evidence from several modalities, including MRI-based measures of function and microstructure, human post-mortem immunohistochemical staining, and cross-species comparison of cortical-NAc projections that are known to be conserved. Finally, we visualize the

Corresponding author: Casey H. Halpern, MD, Department of Neurosurgery, Stanford University, 300 Pasteur Dr. A301, Stanford, CA 94305, Tel: (650) 723-5574, Fax: (650) 725-0390, chalpern@stanford.edu.

passage of individual axon bundles through one NAc subregion in a post-mortem human sample using CLARITY 3D histology corroborated by 7T tractography. Collectively, these findings extensively characterize human NAc subregions and provide insight into their structural and functional distinctions with implications for stereotactic treatments targeting this region.

Keywords

Accumbens; Core; Shell; DBS; Tractography; CLARITY; Computational Modeling

Background

Ample evidence across species has demonstrated the critical role played by the nucleus accumbens (NAc) in mediating reward processing (Haber and Knutson, 2010; Lobo et al., 2010; Thomas et al., 2001). Dysregulation of the NAc is thought to contribute to reward hypersensitivity that is present in many disorders of the brain (Wu et al., 2018). Consequently, the NAc and local region (ventral capsule/ventral striatum) have received considerable attention as therapeutic targets in refractory neuropsychiatric disease (Greenberg et al., 2010; Halpern et al., 2013; Kalivas and Volkow, 2005; Neuner et al., 2009). Nonetheless, substantial variation in clinical outcome exists among patients who undergo neuromodulatory interventions (e.g. deep brain stimulation) of this region (Bergfeld et al., 2016; Denys et al., 2010; Dougherty et al., 2015; Goodman et al., 2010). Even among trials considered to be successful, a substantial fraction of subjects are 'non-responders'. While the source of this variation is multifactorial and may reflect the range of clinical indications for which these treatments are performed, the significance of functional heterogeneity within the NAc itself remains largely unexplored.

There is considerable evidence from studies of rodents and non-human primates to support the notion of distinct functional and structural territories within the NAc. Two primary subregions occupying the dorsolateral and ventromedial portions of the NAc, respectively known as the core and shell, have been identified. These regions are characterized by distinct roles in appetitive behavior (Ambroggi et al., 2011; Ito et al., 2004; Kelley, 2004), patterns of axonal tracer-determined structural connectivity (Groenewegen et al., 1999; Haber et al., 2006; Zahm, 1999), and immunohistochemical reactivity (Meredith et al., 1996; Voorn et al., 1994). Among differences between rodent NAc core and shell fiber pathways are projections from infralimbic cortex (ILC), homologous to the human Brodmann Area 25/subcallosal gyrus (SCG) (Heilbronner et al., 2016), and ventral agranular insula, both of which are largely biased to the shell (Groenewegen et al., 1999; Hamani et al., 2011; Zahm, 1999). These cortico-striatal circuits have strong homology across species, including primates (Fudge et al., 2005; Heilbronner et al., 2016; Jbabdi et al., 2013), whose NAc subregions can also be histochemically differentiated (Meredith et al., 1996; Voorn et al., 1996; Voorn et al., 1994).

Moreover, neuromodulatory interventions in rodent models of neuropsychiatric disease have demonstrated that targeting individual NAc subregions produces dissociable behavioral effects. For instance, deep brain stimulation (DBS) of the NAc shell, but not core, attenuates

binge eating (Halpern et al., 2013) as well as cocaine-related locomotor sensitization(Creed et al., 2015) and reinstatement of drug seeking behavior (Vassoler et al., 2013). Collectively, these studies suggest that some of the observed variability in patient response may be due to non-specific targeting and highlight the need to delineate NAc subregions in humans. However, conventional structural (T_1/ T_2 weighted) imaging used for stereotactic planning cannot reliably localize NAc subregions (Lucas-Neto et al., 2015). Better characterization of this anatomy would further understanding of NAc subregion involvement with existing neuromodulatory targets, permit more precise surgical targeting, improve computational modeling (Gunalan et al., 2018), and bridge preclinical findings specific to these subregions to human neuromodulatory trials.

In the current study, we first motivate the creation of a definitive human NAc segmentation by reporting that the behavioral response to electrical stimulation differs by location within the NAc, whereby greater current is required to produce similar changes in mood and anxiety in a human patient. To achieve our segmentation, we leverage the dissimilar structural connectivity of NAc subregions to cluster the NAc into presumed core and shell using probabilistic tractography, which utilizes diffusion-weighted MRI (dMRI)-based measurements of the movement of water molecules to reconstruct white matter fiber pathways (Behrens et al., 2007; Conturo et al., 1999). We show our segmentation is consistent with the original acute stimulation results, and we explore which white matter pathways may mediate acute effects of DBS stimulation by building a patient-specific model of axonal activation. Using state-of-the-art data from the Human Connectome Project (HCP) (Glasser et al., 2016; Sotiropoulos et al., 2013; Ugurbil et al., 2013), we create an atlas of NAc subregions from the results of 245 subjects' segmentations. We validate our results using a multi-modal approach that includes: (i) comparison against immunohistochemical maps of NAc cytoarchitecture, (ii) dMRI neurite orientation and density imaging measures of tissue microstructure, (iii) functional MRI (fMRI) responses to a gambling task, (iv) comparison to homologous tracts using murine CLARITY 3D histology. We assess the clinical viability of this approach by applying tractography-based segmentation to standard diffusion data, including clinical data acquired as part of routine preoperative stereotactic planning. Finally, we present detailed visualizations of axon bundles projecting through the NAc shell via novel CLARITY-based techniques and highlight the potential applications of these methods.

Methods and Materials

As highlighted in the introduction, several methodological approaches were adopted to explore NAc subregions. These approaches are described in detail below; however, given the range of techniques employed, a brief overview of these methods and their relationship to each other is provided here. First, behavioral responses to acute stimulation of the NAc are reported. Second, a patient-specific computational model of axonal activation in response to stimulation is generated to identify the likely white matter tracts mediating the observed behavioral responses. Third, probabilistic tractography was performed between the NAc and every other gray matter region, and NAc voxels were grouped according their pattern of whole-brain connectivity, yielding 2 distinct subregions (i.e. segmentation). This procedure was performed in several datasets, including a cohort of 245 unrelated healthy subjects from

the HCP whose results were aggregated into a probabilistic atlas that we make available. In the patient who underwent electrical stimulation, this procedure permits localization of subregions relative to active contacts. Fourth, these tractography-defined subregions were validated through a variety of modalities. These modalities include comparison to postmortem immunohistochemistry, MRI measures of structure and function from the HCP dataset, cross-species comparison of subregion-specific NAc-Cortical projections drawn from probabilistic tractography (in humans) and CLARITY-based tractography (in mice). Finally, through a combination of traditional tractography and CLARITY-based techniques we present a unique visualization of axon bundles in a portion of a human postmortem NAc shell.

Response of Human Subject to Acute Monopolar DBS

With IRB approval and patient consent, the effects of acute stimulation of individual DBS lead contacts on self-reported anxiety and mood during initial monopolar testing were assessed on a patient with Tourette Syndrome and co-morbid Obsessive-Compulsive Disorder. The model 3387 lead (Medtronic, Inc., Minneapolis, MN) implanted in this patient off-label contains 4 electrode contacts. The 2 most inferior contacts were located in the NAc bilaterally. The contacts, which are 1.5mm in length, are situated 1.5mm apart along the distal end of the lead. During placement of the leads, consistent with routine clinical practice, the NAc was initially targeted indirectly based on its distance from an anatomical landmark (anterior commissure). The lead trajectories and target were then adjusted to avoid vessels and critical structures.

Anxiety and mood were quantified using a Likert scale with lower scores indicating low anxiety and depressed mood. High scores indicated high anxiety and elevated mood. Individual contacts were tested serially at 0.5V increments, with 1-minute intervals between assessments, and a minimum of 3-minute intervals between testing of each contact to permit restoration of baseline levels of anxiety and mood. The human subject, DBS lead programmer, and data recorder were blinded to the NAc subregion being stimulated.

To assess position of NAc leads and DBS contacts relative to each tractography-defined NAc subregion, postoperative CT images were rigidly co-registered to the patient's structural and diffusion-weighted images using a mutual-information cost function.

Patient-Specific Model of Axon Activation

A two component modeling approach – including a finite element model of the electric field coupled to cable models of myelinated axons - was used to generate a patient-specific model of the most probable subset of axons activated by the implanted DBS leads. First, a model of the electric field was generated using the finite element method implemented in COMSOL Multiphysics v5.3 (COMSOL Inc., Burlington, MA). The skin, skull, and brain layers were segmented from T_1-weighted images using FMRIB Software Library (FSL, https://fsl.fmrib.ox.ac.uk) and imported as the base geometry of the finite element model. Conductivity tensors were defined using the load preservation technique (Howell and McIntyre, 2016) and interpolated onto mesh nodes generated by COMSOL within the modeled brain. This yielded anisotropic white matter, isotropic gray matter, and isotropic

cerebrospinal fluid (CSF) conductivities. All tissues outside the brain were modeled as isotropic (Gunalan et al., 2017). A Medtronic 3387 lead was represented in the model consistent with the patient's post-operative CT registered to T_1 space using a rigid transformation with a mutual information cost function (Maes et al., 1997). A boundary current source of 1 mA was imposed on the active contacts, and since the volume conductor was linear, all potentials scaled directly with the applied current (Pelot et al., 2018). The base of the model was set to zero potential to represent distant current return to the IPG in the chest, the internal boundaries within the model were set to continuity, and the outer boundary was set to a zero current condition. The final mesh had 1,018,746 elements with an average element size of 3.5 mm^3. The highest density of elements was near the 4 electrode contacts where the electric field gradients were the highest. The active contacts were imposed with a boundary current source and the electric potentials were solved throughout the modeled brain. The location of axon tracts originating from the NAc and terminating in brain regions segmented by FreeSurfer software (https://surfer.nmr.mgh.harvard.edu/) was estimated using tractography. Each probabilistic fiber generated using the probtrackx2 command in FSL with the –savepaths flag was defined as a potential model axon. To ensure that the probabilistic fibers best represented realistic axons, the generated streamlines were constrained to project only through known white matter tracts by placing FreeSurfer-defined exclusion masks corresponding to subcortical nuclei between the seeded NAc and the termination brain regions. The probabilistic fibers that remained after this exclusion were subsampled to one hundred fibers for each known fiber bundle associated with the NAc. The electric potentials along the paths of these fibers were determined from the finite element model, and the threshold currents to excite myelinated 2, 3, 4, and 5μm diameter model axons at each fiber location were determined using cable models (McIntyre et al., 2002) implemented in NEURON v7.4.

MRI Data

HCP State-of-the-Art Data: Preprocessed diffusion (from the minimal preprocessing pipeline) and T_1-weighted 3T data from 245 unrelated subjects (55.9% female) were obtained from the publicly available S900 WashU-Minn-Ox HCP dataset (Glasser et al., 2016; Glasser et al., 2013; Sotiropoulos et al., 2013; Van Essen et al., 2012). Additionally, preprocessed and fully analyzed gambling task-related functional data from 850 subjects were obtained. The details of the functional preprocessing and analysis are described in (Barch et al., 2013; Glasser et al., 2013). Briefly, the preprocessing pipeline removes spatial distortions, realigns volumes to compensate for subject motion, registers the fMRI data to the structural, reduces the bias field, normalizes the 4D image to a global mean, and masks the data with the final brain mask. The functional images were then spatially smoothed (FWHM=4mm) and GLM-based analysis was implemented using FSL's FILM. Predictors were convolved with a double gamma HRF and slice-time corrected. A highpass filter was applied and the timeseries was corrected for autocorrelations. Subcortical volumes in MNI152 space were extracted to investigate NAc activity.

Standard Data.—Diffusion and T_1-weighted 3T data were acquired from 2 healthy subjects with Institutional Review Board (IRB) approval and written informed consent.

Patient Data.—Clinical quality diffusion and T_1-weighted 3T data were acquired from a patient suffering from medically intractable TS with co-morbid OCD preoperatively prior to the placement of bilateral NAc DBS leads with IRB approval (IRB-33146) and written informed consent (Medtronic, Inc, Minneapolis, MN, Model 3387, off-label).

A detailed summary of all MRI data is provided in Table 1.

MRI Data Preprocessing

Standard and Patient Data.—For both datasets, the susceptibility-induced off-resonance field and EPI distortion were corrected using FMRIB Software Library's (FSL) 'topup' and 'eddy' functions (Andersson et al., 2003; Smith et al., 2004). The patient's dataset was then upsampled to the resolution of the HCP data (i.e. 1.25 mm isotropic) to facilitate direct comparison and provide finer anatomical detail for subsequent DBS lead localization (Dyrby et al., 2014).

Diffusion MRI Tractography

Given the dissimilar structural connectivity of the NAc subregions, a tractography-based approach is well suited to distinguishing the human core and shell (Lammel et al., 2011). Building a map of tractography-defined fiber pathways between individual voxels within the NAc and the rest of the brain permits characterization of NAc territories with similar structural connectivity (i.e. subregions) (Eickhoff et al., 2015).

The Human Connectome Project (HCP) provides publicly available, state-of-the-art, multimodal MRI data on a large number of subjects (Glasser et al., 2016). Given the NAc's relatively small size (~500–700 mm^3) and the ubiquity of intra-voxel crossing-fibers throughout subcortical white matter, the HCP provides gold-standard dMRI data for mapping NAc structural connectivity and testing functional differences between subregions using functional MRI (fMRI) (Glasser et al., 2013; Jeurissen et al., 2013; Sotiropoulos et al., 2013; Ugurbil et al., 2013).

Tractography Procedure.—All T1-weighted structural images were processed with Freesurfer (https://surfer.nmr.mgh.harvard.edu/) (Fischl, 2012). Cortical gray matter regions of interest (ROIs) were identified from the Desikan Killiany atlas on based on FreeSurfer's parcellation (Desikan et al., 2006); subcortical gray matter ROIs were drawn from (Fischl et al., 2002). A detailed description of the procedure used to generate the NAc ROI in the Freesurfer subcortical atlas is provided in Supplemental Section 1.1. Voxel-wise fiber orientation distributions were estimated using the 'bedpostx' model (fitted with two sticks) from the FMRIB Software Library's (FSL) 'bedpostx' algorithm (Behrens et al., 2007). Probabilistic tractography was performed between the NAc ROI and every ipsilateral cortical and subcortical gray matter ROI defined on the Desikan-Killiany and Freesurfer subcortical atlas using FSL's 'probtrackx2' (Jenkinson et al., 2012). For every target ROI, 5000 streamlines were generated from each voxel in the NAc and only those streamlines that intersected the target ROI were kept. Probabilistic tractography was also performed in the same fashion between NAc voxels and the SCG ROI from Freesurfer's Destrieux atlas (Fischl et al., 2004).

Segmentation

Tractography produced counts of streamlines between each NAc voxel and every ROI. Results from intra-striatal connections were discarded because prior anatomical literature indicates that the caudate and putamen should not be the primary targets that differentiate subregions of the NAc (Groenewegen et al., 1999; Haber and Knutson, 2010; Zahm, 1999), and their close proximity to the NAc potentially confounds tractography-defined connectivity profiles for each subregion. To account for the bias introduced to the tracking algorithm by the differences in distance between the NAc and each ROI, a distance bias correction was implemented (Supplemental Section 1.2). Streamline counts were normalized for each voxel such that the total number of streamlines originating from that voxel was equal to one. Separately for each hemisphere, NAc voxels from all subjects were concatenated and clustered using k-means. Clustering was performed entirely on the basis of each NAc voxel's normalized streamline profile, with no constraints imposed on the spatial contiguity of clusters and no spatial information other than that implicit in the streamlines.

To test the *a priori* hypothesis of two subregions, k-means clustering was performed with k=2, 3…10 subregions, and the appropriateness of the clustering was evaluated using three metrics: the Silhouette criterion, Calinski-Harabasz criterion and elbow plot (Supplemental Section 1.3, Figure S1).

To confirm that segmentation results accurately reflect established fiber pathways, the ratio of streamlines between each NAc subregion and the SCG ROI was computed. This ratio metric additionally permitted comparison of diffusion MRI and CLARITY-based tractography results.

Probabilistic Atlases

Individual HCP subjects' NAc segmentations were non-linearly warped (Supplemental Section 1.4) to a group space (MNI152 NLIN 6th generation) (Grabner et al., 2006)and averaged to create a probabilistic atlas of each NAc subregion (provided in the supplementary materials). The probabilistic atlas permits analysis and visualization of population results. In practice, the atlas can also be co-registered to an individual subject's images to facilitate preoperative target localization in subjects without adequate diffusion data, or to evaluate the location of contacts postoperatively.

An atlas depicting the proportion of subjects who had the same cluster assignment at each voxel was created for each subregion, thus indicating the likelihood of a specific subregion at each NAc voxel (note that to facilitate efficient visualization, Figure 2A shows disjoint results, but these maps are overlapping).

dMRI Microstructure Characterization within Tractography-Defined NAc Subregions

The neurite orientation dispersion and density imaging (NODDI) model (Zhang et al., 2012) was fit to the diffusion MRI data of 245 HCP subjects to assess differences in measures of tissue microstructure between tractography-defined NAc subregions. NODDI models signals from the intracellular compartment, extracellular compartment, and CSF and estimates the fraction of the total volume occupied by neurites (neurite density, ND), the fraction occupied

by CSF (isotropic diffusion, CSF), and the distribution of neurite orientations (orientation dispersion index, ODI). ODI quantifies angular variation of neurite orientation on a scale from zero to one.

fMRI Responses within Tractography-Defined NAc Subregions

Gambling task fMRI data from 850 HCP subjects were used to assess differences in functional responses between tractography-defined NAc subregions. Given that numerous fMRI studies have implicated the NAc in reward-related processing (Cartmell et al., 2014; Knutson et al., 2007), and further that the shell is thought to be preferentially involved in motivational and incentive-related processes (Kelley, 1999; Wyvell and Berridge, 2000), NAc subregion activity was investigated during trials in which subjects won money (Reward versus Baseline). Details of the task design are described in Barch *et al* (2013) (Barch et al., 2013). Briefly, participants play a card guessing game where they are asked to guess the number on a mystery card in order to win or lose money. Subregion activation in the Reward versus Baseline task contrast was examined by averaging the z-scores of each NAc voxel weighted by the probability of membership to either region (determined by the probabilistic atlas) across hemispheres.

Murine CLARITY 3D Histology of NAc Connectivity

Given the well-described input from the SCG to the NAc shell (Haber et al., 2006; Hamani et al., 2011), the infralimbic cortex (ILC, homologous to Brodmann Area 25/SCG in humans) was injected with 0.5 μl of 5×10^{12} genome copies/ml of adeno-associated viral vector at 100nl/min (n=4). This injection induced anterograde expression of green fluorescent protein driven by the CaMKIIa promoter along ILC projection neurons. After 4 weeks, mice were sacrificed with transcardiac perfusion and whole brains were extracted and fixed. The brain tissue was then clarified. Specifics of CLARITY tissue processing methods are detailed in Ye *et* al (Ye et al., 2016).

Microscopic images were acquired with the Ultramicroscope II (LavisionBiotec). Samples were mounted to a custom 3D-printed holder using RapidClear Mounting Gel. Brains were mounted with the ventral side on top. Samples were securely mounted to the holder after the mounting gel solidified (~5 minute at 4°C). Mounted samples were imaged inside an imaging chamber filled with 150ml of RapidClear (reusable by periodical filtering). Samples were left in an imaging chamber for 20–40min before imaging to allow the equilibrium of imaging liquid. Brains were imaged using a 2×/0.5NA objective at 0.6× zoom. All raw images were acquired as 16-bit TIFF files. All experimental protocols were approved by the Stanford Institutional Animal Care and Use Committee and were in accordance with the guidelines from the NIH.

Murine CLARITY Tractography

Fiber pathways between ILC and striatum were evaluated in the mouse using CLARITY-based tractography (http://capture-clarity.org) (Ye et al., 2016). Specifically, 3-dimensional structure tensors were first constructed from CLARITY image intensity gradients. Deterministic tractography streamlines were then generated using the TrackVis software (30˚ angle threshold) from a seed region (defined by stereotaxic injection site, in this case

the ILC). The relative connectivity between the seed site and a given NAc subregion was assessed by computing the ratio of streamlines intersecting each subregion.

Human Postmortem Sample – CLARITY and 7T MRI

Tissue Preparation.—A fresh $2\times1\times1$ cm^3 tissue cuboid was procured from the NAc and embedded it in a 4% acrylamide, 4% PFA hydrogel solution for 1 week. The samples were degased and polymerized at 37°C for 2.5 hours. Excess hydrogel was removed. 7T diffusion and structural MRI data was acquired as described in Table 1. The sample was then cut in half separating the anterior and posterior portions of the NAc. The posterior portion was then cut along a sagittal orientation approximately into thirds, and the middle third containing the internal capsule and portions of the surrounding gray matter was kept. This was further divided along a coronal orientation yielding a sample that was approximately $12 \times 8 \times 0.5$mm. This sample was then passively cleared in a 4% SBC solution for 5 weeks (Tomer et al., 2014). The SBC solution was exchanged every 2 days for the first week and every week thereafter.

Staining.—The SWITCH protocol(Murray et al., 2015) was employed for staining. The sample was stained with Calbindin (ab11426) antibody at a dilution of 1:1000. As a first step we immersed the sample for 20 days into a PBST antibody solution with 1mM SDS and then washed the sample for 4 days in a PBST-antibody solution at 37°C. This was followed by several washing steps in PBST for 10min, 30min, 1h and 3 days. For the secondary antibody we used Alexa Fluor 647 at a dilution of 1:500. We first immersed the samples in a solution containing PBST + secondary antibody = 1mM SDS for 20 days followed by 4 days immersion in a solution containing only PBST + secondary antibody. The secondary antibody was washed off 10min, 30min, 1h and 2days in a PBST solution at 37°C. After clearing the samples were incubated in focusclear for 1 day, mounted on a cover slide and imaged with a confocal microscope with 5x objective.

Registration and Tractography.—The clarified sample was manually coregistered to the 7T structural and diffusion data using a thin plate spline algorithm from the landmark-based registration utility of the MIPAV software package (McAuliffe et al., 2001). The 7T data was then manually registered to the MNI152 brain in the same fashion, permitting evaluation of the location of the sample relative to the probabilistic atlas. Diffusion tensors of the MR acquisition were then computed, and a seed mask for tractography was created in diffusion space based on the 3D extent of the internal capsule in the CLARITY image. Deterministic tractography was then performed using the Diffusion Toolkit software package (45° angle threshold) and results were visualized with TrackVis.

Data and Code Availability

All HCP data used in analyses are publically available at https://www.humanconnectome.org. Patient MR data and human and murine CLARITY data and code used to analyze these data are available upon request.

Results

Monopolar DBS and Patient-Specific Modeling of Axon Activation

Analyses focused on the most ventral contacts, both of which were located in the NAc bilaterally after rigid co-registration of the postoperative CT using a mutual-information cost function. Contacts were present in both NAc subregions on the left, but in only the presumed shell (subregions labeled as described in subsequent results section) on the right (Figure 1A,D). Only standard conventional imaging and stereotactic coordinates based off of the boundaries of this patient's third ventricle were used for preoperative targeting. Tractography results did not inform how this region was targeted surgically. On the left, monopolar stimulation of the contact in the presumed core subregion yielded acute changes in anxiety and mood at currents as low as 1.6 mA, whereas larger currents were required to produce changes in anxiety (3.7 mA) and mood (2.6 mA) following stimulation of the contact in the presumed shell (Figure 1B). No substantial differences were seen between the behavioral responses to stimulation of the two ventral contacts on the right side (Figure 1E).

Computational modeling of the most probable axons activated by stimulation established that at the current threshold required to produce behavioral changes, only axons associated with 3 regions showed at least 50% activation of fibers: the insula, subcallosal gyrus, and the amygdala (Figure 1C,F; Figure S2C,D,E). All other tracts examined required supraphysiologic currents to achieve similar levels of model nerve fiber activation. Furthermore, behavioral trends for stimulation as a function of current amplitude on both sides of the brain best matched input-output curves of model nerve fiber activation for projections from the insula. On the right side, both active contacts had similar insular axon activation profiles. On the left side, significantly more insular axons were activated at lower currents with the anterosuperior contact (located in the presumed core) than with the posteroinferior contact (located in the presumed shell) (Figure 1C,F) consistent with the behavioral data. No other tract tested exhibited a similar asymmetric pattern of activation.

Clustering Results and Probabilistic Atlas

The clustering procedure consistently produced subregions occupying ventral posteromedial and dorsal anterolateral portions of the NAc across subjects. These subregions are evident in the probabilistic atlas (Figure 2A) and in a representative HCP subject (Figure 2B). Where overlap between subjects is maximal, each subregion has a clear locus. Agreement between subjects at these loci was 91% for all subregions. The size of cluster assignments was distributed relatively evenly across all 245 subjects, with the left ventral posteromedial NAc subregion occupying a mean of 60% (Coefficient of variation=0.27) of left whole NAc volume and the right ventral posteromedial subregion occupying an average of 66% (Coefficient of variation=0.24) of right NAc volume. Tractography-based segmentation of conventional and clinical datasets yielded a similar subregion pattern (Fig. 2C,D).

Dorsal anterolateral and ventral posteromedial subregions from this atlas showed strong agreement with studies of non-human primates and previously published human histological sections that demarcated putative core and shell territories (Figure 2E,F) (Meredith et al., 1996; Voorn et al., 1996). For concision, subsequently the tractography-defined dorsal

anterolateral and ventral posteromedial subregions are referred to as presumed core and shell, respectively.

Connections of the Human Nucleus Accumbens

The connectivity between the whole NAc and cortical and subcortical ROIs was considered first. The results of this analysis, averaged across hemispheres (Figure 3A), revealed that the medial orbitofrontal cortex (mOFC) provides the largest proportion of streamlines to the NAc, followed by the insula, ventral diencephalon (a region which in the Freesurfer ontology includes hypothalamus and ventral tegmental area), lateral OFC, and thalamus, consistent with known tracts involving the NAc (Fischl et al., 2002; Haber and Knutson, 2010). When separated by hemisphere, connectivity of the left and right NAc was virtually identical with two notable exceptions: mOFC-NAc fiber projections made up a larger proportion of the total number of streamlines on the left as compared to the right. The opposite pattern was observed for pathways involving the NAc and insula, where the probability of a fiber pathway between the right NAc and insula was greater than that of the left, suggesting hemispheric laterality differences (Figure 3B).

Pathways associated with each tractography-defined NAc subregion were examined next. The insula and temporal pole had a greater proportion of streamlines intersecting the presumed shell, whereas the thalamus, lateral OFC, and dorsal prefrontal regions (rostral middle frontal gyrus and frontal pole) had greater proportions of streamlines from presumed core (Figure 3C,D). While pathways from each subregion to the rest of the brain were largely similar across hemispheres, asymmetry was also present. Specifically, the mOFC was the only region with robust connectivity to the NAc (i.e. streamlines constituting >5% of the total bilaterally) that demonstrated asymmetric connectivity to subregions—mOFC fibers projected preferentially to the presumed shell on the left, but to the presumed core on the right.

At its posterior aspect, the mOFC FreeSurfer ROI includes a large fraction of voxels that belong to the SCG, which, along with the homologous region known as the infralimbic cortex (ILC) in rodents, is known to project specifically the shell (Haber et al., 2006; Hamani et al., 2011). To ensure that the observed relationship between the right mOFC and presumed core was not spurious, the ratio of streamlines from the SCG to each subregion was computed for both hemispheres. This demonstrated highly biased input from SCG to presumed shell bilaterally (Figure 3E). Moreover, these findings confirmed that segmentation results are consistent with prior understanding of this circuitry, and suggested observed asymmetries are driven by streamlines from regions of mOFC anterior to SCG (Haber et al., 2006; Hamani et al., 2011).

Diffusion MRI Microstructure and Functional MRI Within Tractography-Defined NAc Subregions

Diffusion MRI Microstructure.—Subregions designated by cluster output differed in every measure of tissue microstructure calculated by the NODDI model. The absolute differences were small but extremely consistent across subjects and statistically robust. Specifically, differences were observed in neurite density (ND) (presumed shell mean ND =

0.4899, presumed core mean ND = 0.4967, t(1,244) = 6.013, p < 0.0001); orientation dispersion index (ODI), which quantifies angular variation of neurite orientation (mean presumed shell ODI = 0.4967, mean presumed core ODI = 0.5178, t(1,244) = 10.63, p < 0.0001); and CSF volume fraction (mean presumed shell CSF fraction = 0.0865, mean presumed core CSF fraction = 0.07389, t(1,244) = 7.598, p < 0.0001).

Functional MRI.—Presumed shell and core subregions had significantly different responses to reward as measured by fMRI responses during the gambling task. Consistent with the hypothesis that the shell is preferentially involved in reward anticipation and incentive motivation (Kelley, 2004), activity in the presumed shell was greater during the experience of reward than at baseline (mean z-scores, presumed shell = 0.04, presumed core = 0.02, t(1,849) = 2.87, p < 0.005).

Murine CLARITY Tractography

In all mice, a large projection from the ILC to the ventromedial NAc (well-defined in the mouse brain as the shell subregion) was identified as expected(Haber et al., 2006), and confirmed the homology of the biased projection profile of the ILC and the human SCG. A smaller tract traveled to the core subregion in the dorsal portion of the NAc immediately adjacent to the anterior commissure (Figure 4B–E) (Paxinos and Franklin, 2004). Evaluation of the ratio of streamlines passing through NAc shell and core in mice (4.56:1) revealed a qualitatively similar bias as that present in streamlines from the SCG to the presumed shell and presumed core NAc in humans (11.7:1, Figure 3E).

Human Postmortem Sample

CLARITY.—The 500μm sample was successfully cleared and stained with calbindin and secondary antibodies. Registration with the probabilistic atlas indicated the clarified tissue came primarily from the presumed shell, which is relatively calbindin-poor, consistent with the staining pattern. Conversely, the internal capsule and other presumed white matter fibers present in the clarified tissue displayed strong autofluorescence, permitting the visualization of axon bundles (Figure 5C; Video 1). Using autofluoresence to identify myelin-rich structures after fixation is consistent with previous reports taking advantage of this property to study axon morphology (Christensen et al., 2014). This projection permits direct visual confirmation of fibers defined indirectly by tractography, including both those caught in cross-section and those oriented horizontally in the clarified sample.

Tractography.—Using a seed mask corresponding to the volume of white matter (i.e internal capsule) present in the clarified sample, a robust set of fibers can be visualized. Consistent with visual inspection of the clarified sample, fiber bundles can be seen in transit to and from the adjacent internal capsule. Several fibers can be seen traversing in a medial-to-lateral and inferior-superior orientation, in contrast to the primarily anterior-posterior orientation of the bulk of the capsule fibers.

Discussion

Extending the considerable evidence for distinct subregions in rodents and non-human primates, the current study first demonstrated that the different locations within the NAc require differing levels of electrical stimulation to produce similar affective changes in a human patient. Motivated by these findings, we established that connectivity profiles of individual voxels can be used to reliably segment the NAc into dorsal anterolateral (presumed core) and ventral posteromedial (presumed shell) subregions across datasets. These tractography-defined subregions closely match postmortem immunohistochemical staining data demarcating putative core and shell in humans (Haber and Knutson, 2010; Meredith et al., 1996; Voorn et al., 1996), can account for the observed behavioral responses to monopolar DBS, and are further supported by MRI-based measures of function during a gambling task and diffusion microstructure (NODDI). Given the prominence of the NAc shell in reward-related behavior, these results are important because they support the notion that this segmentation is accurate and functionally relevant. Moreover, the observed structural differences raise the possibility that structural imaging may be able to resolve these subregions directly without the need for tractography in the future. To further validate our results, we examine cortical-NAc projections that are known to be conserved across species through a novel comparison of human diffusion and murine CLARITY-based tractography and find the degree of subregion selectivity to be highly concordant. These findings allow us to more confidently define our segmentation as accurately reflecting the human core and shell subregions. Finally, we visualize and characterize fibers traversing the shell through novel methods, including one of the first applications of CLARITY in human tissue.

Our results underscore the prominence of connections between the NAc and cortical areas, in particular between both the mOFC and insula—a tract that was only recently described (Leong et al., 2016). Both cortical areas have been strongly implicated in reward-related behavior and decision-making (Bossaerts, 2010; Gottfried et al., 2003; O'Doherty et al., 2001). The existence of robust structural connectivity (indexed by large relative streamline probabilities) itself indicates the importance of the NAc, and in particular the NAc shell, in mediating these processes. The functional importance of these connections is supported by the results of the patient-specific model of axonal activation, which suggests recruitment of insular fibers mediates acute changes in affect following monopolar NAc DBS. Nonetheless, these findings also raise questions with regard to the observed asymmetries in streamline probabilities from the insula and mOFC to the NAc as a whole. NAc-mOFC asymmetries, in particular between the NAc and anteriorly-located regions of mOFC, may also extend to individual NAc subregions. The significance of these previously unreported asymmetries is currently uncertain, but they suggest that lateralization may extend to deep structures involved with fundamental processes such as those related to reward. Moreover, a better understanding of the circuit involved in these processes may lead to improved interventional treatments of diseases involving these circuits.

Prior studies have used diffusion tractography to distinguish subregions of the NAc. However, early attempts were limited by small sample sizes, low spatial resolution, acquisition parameters that are not suited to model crossing fibers, or results that are

incongruent with reported structural anatomy (Baliki et al., 2013; Lucas-Neto et al., 2015). We circumvent these issues by using data from a large HCP cohort. Our results demonstrate robust agreement with known fiber pathways and concordance with immunohistochemical results, especially in the anterior, lateral, and ventral extension of the shell. A recent study by Xia *et al.* used HCP data from fewer subjects to subdivide the NAc (Xia et al., 2017). However, in contrast to the Xia study, we leverage the very large number of subjects in our dataset by pooling all subjects' data prior to performing the clustering procedure, thus minimizing uncertainty generated during the acquisition and processing pipeline to produce greater signal. Their results demonstrated a similar topographical distribution to our own, providing convergent evidence for the existence and location of this division. However, we report novel asymmetries in the connectivity profiles of the NAc and its subregions (Figure 3), and furnish evidence that adding more subjects meaningfully affects subregion assignment (Figure S3). Furthermore, the success of performing clustering at the group level itself provides evidence, not directly apparent from averaging individual results, that NAc subregion structural connectivity profiles are similar across subjects. Meanwhile, the high degree of spatial concordance across subjects indicates NAc subregions are also highly similar in location between individuals. In addition, we produce a probabilistic atlas based on all 245 subjects' results that can facilitate stereotactic targeting to optimize surgical outcomes in future trials.

These results have implications for neurosurgical therapies such as DBS. The DBS experience in movement disorders suggests that even 2 mm of targeting error can negatively affect outcome, and tractography exhibits promise in ameliorating this error by identification of relevant fiber pathways (Anheim et al., 2008; Henderson, 2012; Richardson et al., 2009). Our approach represents an additional step in tractography image guidance, and our findings provisionally suggest ways in which efficacy may be improved over DBS studies targeting the NAc region (Dougherty et al., 2015). Further, through our clarified human NAc sample and corroborating 7T tractography, we provide a novel and direct visualization of fibers as they traverse the NAc shell and join the ventral internal capsule. These fibers likely represent efferents travelling dorsally from the portion of ventromedial prefrontal cortex situated inferiorly to the NAc. Tracer studies have established the presence of these efferents in macaques but prior human in-vivo tractography has been unable to model these small fibers, which are embedded relatively isotropic gray matter (Jbabdi et al., 2013).

Given the interest in using DBS to target the NAc, results from the clarified human tissue represent meaningful steps to characterize important anatomical features of this region, such as the precise location and orientation of axon bundles. Since such features are crucial to the electrical properties of the tissue, and thus the response to DBS, (Grill, 1999) it will be important to incorporate these results in future models, particularly as the ability to clarify larger volumes of tissue is achieved. Future work in clinical trials will be required to develop rigorously electrodes best tailored to NAc subregions, investigate subregion-specific, long-term stimulatory effects in a larger cohort, and confirm the tracts involved in mediating behavioral effects of DBS (Howell et al., 2015).

Inferences regarding reported fiber pathways involving the NAc are dependent on the accuracy and consistency of FreeSurfer's automated parcellation. For instance, should

FreeSurfer mOFC estimation be systematically different between hemispheres, this could drive the asymmetries reported above. Nonetheless, suspicion for such a cause is low, as mOFC and insula volumes are similar between hemispheres (Figure S4), and to the authors' knowledge such systematic asymmetries have not been reported in the period since FreeSurfer's release over a decade ago (Dale et al., 1999). Indeed, because identical analyses were conducted in each hemisphere, results from the contralateral side effectively serve as an internal control. Relatedly, imprecision in the boundaries of the NAc ROI could result in partial volume effects that distort the fMRI and dMRI microstructure results.

Aside from hemispheric differences in streamline probabilities, segmentation itself may be affected by the choice of atlas. The Desikan-Killiany atlas used in this analysis is based on anatomy and thus may miss important distinctions based on function that may be reflected in other atlases. Moreover, although we readily observed streamlines targeting the presumed shell from the SCG in a similar pattern to NAc-ILC fibers observed in the rodent, several exclusive connections known to exist between the shell and other regions (e.g. medial subdivision of the central nucleus of amygdala) (Groenewegen et al., 1999; Haber and Knutson, 2010) were not specifically visualized, nor did the amygdala or hippocampus seem to play a large role in segmentation. This may reflect that FreeSurfer does not currently segment individual nuclei of the amygdala or that additional, non-subregion-specific pathways emanate from nearby territories within the same structures. Nonetheless, despite concerns related to the use of an anatomy-based atlas that lacks hippocampal and amygdalar sub-nuclei that may enjoy special connections to NAc subregions, we achieve excellent concordance with immunohistochemical results.

Supplementary Material

Refer to Web version on PubMed Central for supplementary material.

ACKNOWLEDGEMENTS

REFERENCES

Ambroggi F, Ghazizadeh A, Nicola SM, Fields HL, 2011 Roles of nucleus accumbens core and shell in incentive-cue responding and behavioral inhibition. J Neurosci 31, 6820–6830. [PubMed: 21543612]

Andersson JLR, Skare S, Ashburner J, 2003 How to correct susceptibility distortions in spin-echo echo-planar images: application to diffusion tensor imaging. Neuroimage 20, 870–888. [PubMed: 14568458]

Anheim M, Batir A, Fraix V, Silem M, Chabardès S, Seigneuret E, Krack P, Benabid A-L, Pollak P, 2008 Improvement in Parkinson disease by subthalamic nucleus stimulation based on electrode placement: effects of reimplantation. Archives of neurology 65, 612–616. [PubMed: 18474736]

Baliki MN, Mansour A, Baria AT, Huang L, Berger SE, Fields HL, Apkarian AV, 2013 Parceling human accumbens into putative core and shell dissociates encoding of values for reward and pain. The Journal of Neuroscience 33, 16383–16393. [PubMed: 24107968]

Barch DM, Burgess GC, Harms MP, Petersen SE, Schlaggar BL, Corbetta M, Glasser MF, Curtiss S, Dixit S, Feldt C, 2013 Function in the human connectome: task-fMRI and individual differences in behavior. Neuroimage 80, 169–189. [PubMed: 23684877]

Behrens TE, Berg HJ, Jbabdi S, Rushworth M, Woolrich M, 2007 Probabilistic diffusion tractography with multiple fibre orientations: What can we gain? Neuroimage 34, 144–155. [PubMed: 17070705]

Bergfeld IO, Mantione M, Hoogendoorn ML, Ruhé HG, Notten P, van Laarhoven J, Visser I, Figee M, de Kwaasteniet BP, Horst F, 2016 Deep brain stimulation of the ventral anterior limb of the internal capsule for treatment-resistant depression: a randomized clinical trial. JAMA psychiatry 73, 456–464. [PubMed: 27049915]

Bossaerts P, 2010 Risk and risk prediction error signals in anterior insula. Brain Structure and Function 214, 645–653. [PubMed: 20512378]

Cartmell SC, Chun MM, Vickery TJ, 2014 Neural antecedents of social decision-making in a partner choice task. Soc Cogn Affect Neurosci 9, 1722–1729. [PubMed: 24194578]

Christensen PC, Brideau C, Poon KW, Doring A, Yong VW, Stys PK, 2014 High-resolution fluorescence microscopy of myelin without exogenous probes. Neuroimage 87, 42–54. [PubMed: 24188810]

Conturo TE, Lori NF, Cull TS, Akbudak E, Snyder AZ, Shimony JS, McKinstry RC, Burton H, Raichle ME, 1999 Tracking neuronal fiber pathways in the living human brain. Proceedings of the National Academy of Sciences 96, 10422–10427.

Creed M, Pascoli VJ, Lüscher C, 2015 Refining deep brain stimulation to emulate optogenetic treatment of synaptic pathology. Science 347, 659–664. [PubMed: 25657248]

Dale AM, Fischl B, Sereno MI, 1999 Cortical surface-based analysis: I. Segmentation and surface reconstruction. Neuroimage 9, 179–194. [PubMed: 9931268]

Denys D, Mantione M, Figee M, van den Munckhof P, Koerselman F, Westenberg H, Bosch A, Schuurman R, 2010 Deep brain stimulation of the nucleus accumbens for treatment-refractory obsessive-compulsive disorder. Archives of general psychiatry 67, 1061–1068. [PubMed: 20921122]

Desikan RS, Segonne F, Fischl B, Quinn BT, Dickerson BC, Blacker D, Buckner RL, Dale AM, Maguire RP, Hyman BT, Albert MS, Killiany RJ, 2006 An automated labeling system for subdividing the human cerebral cortex on MRI scans into gyral based regions of interest. Neuroimage 31, 968–980. [PubMed: 16530430]

Dougherty DD, Rezai AR, Carpenter LL, Howland RH, Bhati MT, O'Reardon JP, Eskandar EN, Baltuch GH, Machado AD, Kondziolka D, Cusin C, Evans KC, Price LH, Jacobs K, Pandya M, Denko T, Tyrka AR, Brelje T, Deckersbach T, Kubu C, Malone DA Jr., 2015 A Randomized Sham-Controlled Trial of Deep Brain Stimulation of the Ventral Capsule/Ventral Striatum for Chronic Treatment-Resistant Depression. Biol Psychiatry 78, 240–248. [PubMed: 25726497]

Dyrby TB, Lundell H, Burke MW, Reislev NL, Paulson OB, Ptito M, Siebner HR, 2014 Interpolation of diffusion weighted imaging datasets. Neuroimage 103, 202–213. [PubMed: 25219332]

Eickhoff SB, Thirion B, Varoquaux G, Bzdok D, 2015 Connectivity-based parcellation: Critique and implications. Hum Brain Mapp 36, 4771–4792. [PubMed: 26409749]

Fischl B, 2012 FreeSurfer. Neuroimage 62, 774–781. [PubMed: 22248573]

Fischl B, Salat DH, Busa E, Albert M, Dieterich M, Haselgrove C, Van Der Kouwe A, Killiany R, Kennedy D, Klaveness S, 2002 Whole brain segmentation: automated labeling of neuroanatomical structures in the human brain. Neuron 33, 341–355. [PubMed: 11832223]

Fischl B, Van Der Kouwe A, Destrieux C, Halgren E, Ségonne F, Salat DH, Busa E, Seidman LJ, Goldstein J, Kennedy D, 2004 Automatically parcellating the human cerebral cortex. Cerebral cortex 14, 11–22. [PubMed: 14654453]

Fudge JL, Breitbart MA, Danish M, Pannoni V, 2005 Insular and gustatory inputs to the caudal ventral striatum in primates. Journal of Comparative Neurology 490, 101–118. [PubMed: 16052493]

Glasser MF, Coalson TS, Robinson EC, Hacker CD, Harwell J, Yacoub E, Ugurbil K, Andersson J, Beckmann CF, Jenkinson M, Smith SM, Van Essen DC, 2016 A multi-modal parcellation of human cerebral cortex. Nature 536, 171–178. [PubMed: 27437579]

Glasser MF, Sotiropoulos SN, Wilson JA, Coalson TS, Fischl B, Andersson JL, Xu J, Jbabdi S, Webster M, Polimeni JR, Van Essen DC, Jenkinson M, 2013 The minimal preprocessing pipelines for the Human Connectome Project. Neuroimage 80, 105–124. [PubMed: 23668970]

Goodman WK, Foote KD, Greenberg BD, Ricciuti N, Bauer R, Ward H, Shapira NA, Wu SS, Hill CL, Rasmussen SA, 2010 Deep brain stimulation for intractable obsessive compulsive disorder: pilot study using a blinded, staggered-onset design. Biological Psychiatry 67, 535–542. [PubMed: 20116047]

Gottfried JA, O'Doherty J, Dolan RJ, 2003 Encoding predictive reward value in human amygdala and orbitofrontal cortex. Science 301, 1104–1107. [PubMed: 12934011]

Grabner G, Janke AL, Budge MM, Smith D, Pruessner J, Collins DL, 2006 Symmetric atlasing and model based segmentation: an application to the hippocampus in older adults. Med Image Comput Comput Assist Interv 9, 58–66.

Greenberg BD, Gabriels LA, Malone DA Jr., Rezai AR, Friehs GM, Okun MS, Shapira NA, Foote KD, Cosyns PR, Kubu CS, Malloy PF, Salloway SP, Giftakis JE, Rise MT, Machado AG, Baker KB, Stypulkowski PH, Goodman WK, Rasmussen SA, Nuttin BJ, 2010 Deep brain stimulation of the ventral internal capsule/ventral striatum for obsessive-compulsive disorder: worldwide experience. Mol Psychiatry 15, 64–79. [PubMed: 18490925]

Grill WM, 1999 Modeling the effects of electric fields on nerve fibers: influence of tissue electrical properties. IEEE Transactions on Biomedical Engineering 46, 918–928. [PubMed: 10431456]

Groenewegen HJ, Wright CI, Beijer AV, Voorn P, 1999 Convergence and segregation of ventral striatal inputs and outputs. Annals of the New York Academy of Sciences 877, 49–63. [PubMed: 10415642]

Gunalan K, Chaturvedi A, Howell B, Duchin Y, Lempka SF, Patriat R, Sapiro G, Harel N, McIntyre CC, 2017 Creating and parameterizing patient-specific deep brain stimulation pathway-activation models using the hyperdirect pathway as an example. PloS one 12, e0176132. [PubMed: 28441410]

Gunalan K, Howell B, McIntyre CC, 2018 Quantifying axonal responses in patient-specific models of subthalamic deep brain stimulation. Neuroimage 172, 263–277. [PubMed: 29331449]

Haber SN, Kim KS, Mailly P, Calzavara R, 2006 Reward-related cortical inputs define a large striatal region in primates that interface with associative cortical connections, providing a substrate for incentive-based learning. J Neurosci 26, 8368–8376. [PubMed: 16899732]

Haber SN, Knutson B, 2010 The reward circuit: linking primate anatomy and human imaging. Neuropsychopharmacology 35, 4–26. [PubMed: 19812543]

Halpern CH, Tekriwal A, Santollo J, Keating JG, Wolf JA, Daniels D, Bale TL, 2013 Amelioration of binge eating by nucleus accumbens shell deep brain stimulation in mice involves D2 receptor modulation. J Neurosci 33, 7122–7129. [PubMed: 23616522]

Hamani C, Mayberg H, Stone S, Laxton A, Haber S, Lozano AM, 2011 The subcallosal cingulate gyrus in the context of major depression. Biol Psychiatry 69, 301–308. [PubMed: 21145043]

Heilbronner SR, Rodriguez-Romaguera J, Quirk GJ, Groenewegen HJ, Haber SN, 2016 Circuit-Based Corticostriatal Homologies Between Rat and Primate. Biol Psychiatry 80, 509–521. [PubMed: 27450032]

Henderson JM, 2012 Connectomic surgery: diffusion tensor imaging (DTI) tractography as a targeting modality for surgical modulation of neural networks. Front Integr Neurosci 6, 3389.

Howell B, Huynh B, Grill WM, 2015 Design and in vivo evaluation of more efficient and selective deep brain stimulation electrodes. Journal of neural engineering 12, 046030. [PubMed: 26170244]

Howell B, McIntyre CC, 2016 Analyzing the tradeoff between electrical complexity and accuracy in patient-specific computational models of deep brain stimulation. Journal of neural engineering 13, 036023. [PubMed: 27172137]

Ito R, Robbins TW, Everitt BJ, 2004 Differential control over cocaine-seeking behavior by nucleus accumbens core and shell. Nat Neurosci 7, 389–397. [PubMed: 15034590]

Jbabdi S, Lehman JF, Haber SN, Behrens TE, 2013 Human and monkey ventral prefrontal fibers use the same organizational principles to reach their targets: tracing versus tractography. J Neurosci 33, 3190–3201. [PubMed: 23407972]

Jenkinson M, Beckmann CF, Behrens TE, Woolrich MW, Smith SM, 2012 FSL. Neuroimage 62, 782–790. [PubMed: 21979382]

Jeurissen B, Leemans A, Tournier JD, Jones DK, Sijbers J, 2013 Investigating the prevalence of complex fiber configurations in white matter tissue with diffusion magnetic resonance imaging. Hum Brain Mapp 34, 2747–2766. [PubMed: 22611035]

Kalivas PW, Volkow ND, 2005 The neural basis of addiction: a pathology of motivation and choice. American Journal of Psychiatry 162, 1403–1413. [PubMed: 16055761]

Kelley AE, 1999 Functional specificity of ventral striatal compartments in appetitive behaviors. Annals of the New York Academy of Sciences 877, 71–90. [PubMed: 10415644]

Kelley AE, 2004 Ventral striatal control of appetitive motivation: role in ingestive behavior and reward-related learning. Neurosci Biobehav Rev 27, 765–776. [PubMed: 15019426]

Knutson B, Rick S, Wimmer GE, Prelec D, Loewenstein G, 2007 Neural predictors of purchases. Neuron 53, 147–156. [PubMed: 17196537]

Lammel S, Ion DI, Roeper J, Malenka RC, 2011 Projection-specific modulation of dopamine neuron synapses by aversive and rewarding stimuli. Neuron 70, 855–862. [PubMed: 21658580]

Leong JK, Pestilli F, Wu CC, Samanez-Larkin GR, Knutson B, 2016 White-Matter Tract Connecting Anterior Insula to Nucleus Accumbens Correlates with Reduced Preference for Positively Skewed Gambles. Neuron 89, 63–69. [PubMed: 26748088]

Lobo MK, Covington HE, Chaudhury D, Friedman AK, Sun H, Damez-Werno D, Dietz DM, Zaman S, Koo JW, Kennedy PJ, 2010 Cell type–specific loss of BDNF signaling mimics optogenetic control of cocaine reward. Science 330, 385–390. [PubMed: 20947769]

Lucas-Neto L, Reimao S, Oliveira E, Rainha-Campos A, Sousa J, Nunes RG, Goncalves-Ferreira A, Campos JG, 2015 Advanced MR Imaging of the Human Nucleus Accumbens--Additional Guiding Tool for Deep Brain Stimulation. Neuromodulation 18, 341–348. [PubMed: 25879622]

Maes F, Collignon A, Vandermeulen D, Marchal G, Suetens P, 1997 Multimodality image registration by maximization of mutual information. IEEE transactions on Medical Imaging 16, 187–198. [PubMed: 9101328]

McAuliffe MJ, Lalonde FM, McGarry D, Gandler W, Csaky K, Trus BL, 2001 Medical image processing, analysis and visualization in clinical research. Computer-Based Medical Systems, 2001. CBMS 2001. Proceedings 14th IEEE Symposium on. IEEE, pp. 381–386.

McIntyre CC, Richardson AG, Grill WM, 2002 Modeling the excitability of mammalian nerve fibers: influence of afterpotentials on the recovery cycle. J Neurophysiol 87, 995–1006. [PubMed: 11826063]

Meredith G, Pattiselanno A, Groenewegen H, Haber S, 1996 Shell and Core in Monkey and Human. THE JOURNAL, OF COMPARATIVE NEUROLOGY 365, 628–639. [PubMed: 8742307]

Murray E, Cho JH, Goodwin D, Ku T, Swaney J, Kim S-Y, Choi H, Park Y-G, Park J-Y, Hubbert A, 2015 Simple, scalable proteomic imaging for high-dimensional profiling of intact systems. Cell 163, 1500–1514. [PubMed: 26638076]

Neuner I, Podoll K, Lenartz D, Sturm V, Schneider F, 2009 Deep brain stimulation in the nucleus accumbens for intractable Tourette's syndrome: follow-up report of 36 months. Biological Psychiatry 65, e5–e6. [PubMed: 19006786]

O'Doherty J, Kringelbach ML, Rolls ET, Hornak J, Andrews C, 2001 Abstract reward and punishment representations in the human orbitofrontal cortex. Nat Neurosci 4, 95. [PubMed: 11135651]

Paxinos G, Franklin KB, 2004 The mouse brain in stereotaxic coordinates. Gulf Professional Publishing.

Pelot NA, Thio BJ, Grill WM, 2018 Modeling current sources for neural stimulation in COMSOL. Front Comput Neurosci 12, 40. [PubMed: 29937722]

Richardson RM, Ostrem JL, Starr PA, 2009 Surgical repositioning of misplaced subthalamic electrodes in Parkinson's disease: location of effective and ineffective leads. Stereotactic and functional neurosurgery 87, 297–303. [PubMed: 19641340]

Smith SM, Jenkinson M, Woolrich MW, Beckmann CF, Behrens TE, Johansen-Berg H, Bannister PR, De Luca M, Drobnjak I, Flitney DE, Niazy RK, Saunders J, Vickers J, Zhang Y, De Stefano N, Brady JM, Matthews PM, 2004 Advances in functional and structural MR image analysis and implementation as FSL. Neuroimage 23 Suppl 1, S208–219.

Sotiropoulos SN, Jbabdi S, Xu J, Andersson JL, Moeller S, Auerbach EJ, Glasser MF, Hernandez M, Sapiro G, Jenkinson M, Feinberg DA, Yacoub E, Lenglet C, Van Essen DC, Ugurbil K, Behrens TE, Consortium WU-MH, 2013 Advances in diffusion MRI acquisition and processing in the Human Connectome Project. Neuroimage 80, 125–143. [PubMed: 23702418]

Thomas MJ, Beurrier C, Bonci A, Malenka RC, 2001 Long-term depression in the nucleus accumbens: a neural correlate of behavioral sensitization to cocaine. Nat Neurosci 4, 1217–1223. [PubMed: 11694884]

Tomer R, Ye L, Hsueh B, Deisseroth K, 2014 Advanced CLARITY for rapid and high-resolution imaging of intact tissues. Nature protocols 9, 1682. [PubMed: 24945384]

Ugurbil K, Xu J, Auerbach EJ, Moeller S, Vu AT, Duarte-Carvajalino JM, Lenglet C, Wu X, Schmitter S, Van de Moortele PF, Strupp J, Sapiro G, De Martino F, Wang D, Harel N, Garwood M, Chen L, Feinberg DA, Smith SM, Miller KL, Sotiropoulos SN, Jbabdi S, Andersson JL, Behrens TE, Glasser MF, Van Essen DC, Yacoub E, Consortium WU-MH, 2013 Pushing spatial and temporal resolution for functional and diffusion MRI in the Human Connectome Project. Neuroimage 80, 80–104. [PubMed: 23702417]

Van Essen DC, Ugurbil K, Auerbach E, Barch D, Behrens TE, Bucholz R, Chang A, Chen L, Corbetta M, Curtiss SW, Della Penna S, Feinberg D, Glasser MF, Harel N, Heath AC, Larson-Prior L, Marcus D, Michalareas G, Moeller S, Oostenveld R, Petersen SE, Prior F, Schlaggar BL, Smith SM, Snyder AZ, Xu J, Yacoub E, Consortium WU-MH, 2012 The Human Connectome Project: a data acquisition perspective. Neuroimage 62, 2222–2231. [PubMed: 22366334]

Vassoler FM, White SL, Hopkins TJ, Guercio LA, Espallergues J, Berton O, Schmidt HD, Pierce RC, 2013 Deep brain stimulation of the nucleus accumbens shell attenuates cocaine reinstatement through local and antidromic activation. Journal of Neuroscience 33, 14446–14454. [PubMed: 24005296]

Voorn P, Brady L, Berendse H, Richfield E, 1996 Densitometrical analysis of opioid receptor ligand binding in the human striatum—I. Distribution of μ opioid receptor defines shell and core of the ventral striatum. Neuroscience 75, 777–792. [PubMed: 8951872]

Voorn P, Brady L, Schotte A, Berendse H, Richfield E, 1994 Evidence for two neurochemical divisions in the human nucleus accumbens. Eur J Neurosci 6, 1913–1916. [PubMed: 7704301]

Wu H, Miller KJ, Blumenfeld Z, Williams NR, Ravikumar VK, Lee KE, Kakusa B, Sacchet MD, Wintermark M, Christoffel DJ, 2018 Closing the loop on impulsivity via nucleus accumbens delta-band activity in mice and man. Proceedings of the National Academy of Sciences 115, 192–197.

Wyvell CL, Berridge KC, 2000 Intra-accumbens amphetamine increases the conditioned incentive salience of sucrose reward: enhancement of reward "wanting" without enhanced "liking" or response reinforcement. Journal of Neuroscience 20, 8122–8130. [PubMed: 11050134]

Xia X, Fan L, Cheng C, Eickhoff SB, Chen J, Li H, Jiang T, 2017 Multimodal connectivity-based parcellation reveals a shell-core dichotomy of the human nucleus accumbens. Hum Brain Mapp.

Ye L, Allen WE, Thompson KR, Tian Q, Hsueh B, Ramakrishnan C, Wang AC, Jennings JH, Adhikari A, Halpern CH, Witten IB, Barth AL, Luo L, McNab JA, Deisseroth K, 2016 Wiring and Molecular Features of Prefrontal Ensembles Representing Distinct Experiences. Cell 165, 1776–1788. [PubMed: 27238022]

Zahm DS, 1999 Functional - anatomical Implications of the Nucleus Accumbens Core and Shell Subterritories. Annals of the New York Academy of Sciences 877, 113–128. [PubMed: 10415646]

Zhang H, Schneider T, Wheeler-Kingshott CA, Alexander DC, 2012 NODDI: practical in vivo neurite orientation dispersion and density imaging of the human brain. Neuroimage 61, 1000–1016. [PubMed: 22484410]
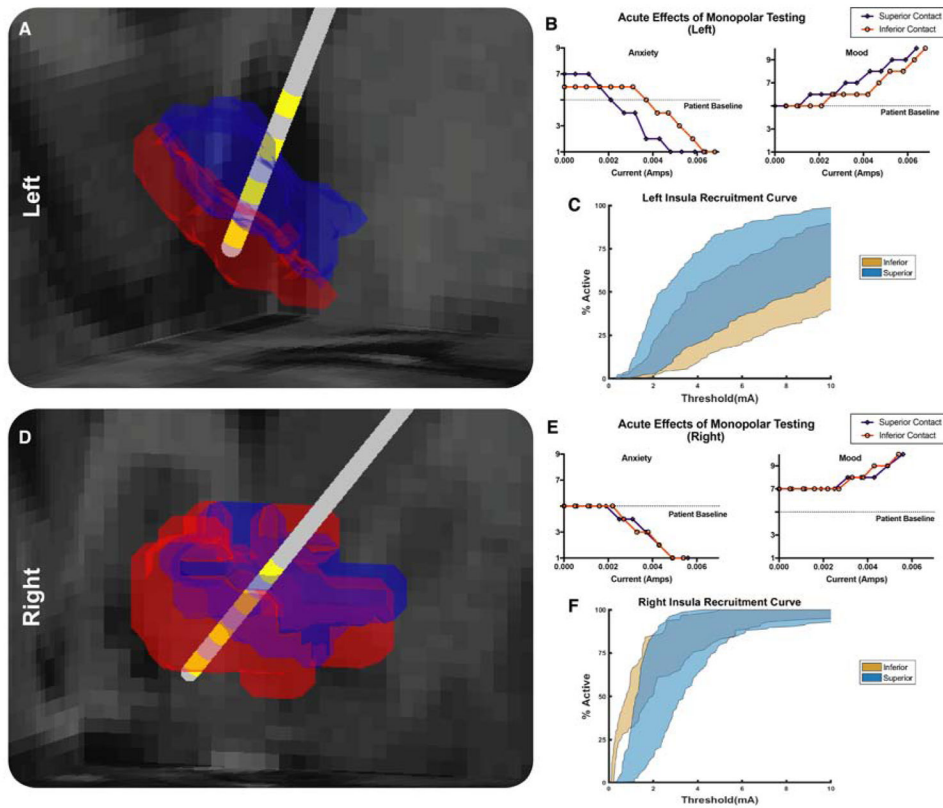
Figure 1. Volume-based representation of DBS contacts' locations relative to NAc subregions and associated affective changes.

Analyses focus on 2 most ventral contacts, which were found to be located in NAc bilaterally. **A** Left NAc subregions computed from clinical dataset shown (presumed core in blue, shell in red) relative to DBS lead (grey) and location of electrical contacts (yellow). Left presumed core overlaps with superior contact (contact 1), and left presumed shell subregion overlaps with inferior contact (contact 0). AP view. **B** The acute effects of stimulation of each contact in the left NAc on self-reported anxiety and mood. **C** Recruitment curves of left NAc-insula fibers derived from patient-specific computational model of axonal activation in response to monopolar stimulation. **D** As in **A,** right NAc subregions shown (presumed core in blue, presumed shell in red) relative to DBS lead (grey) and location of electrical contacts (yellow). Two most ventral contacts (contact 0, labeled 'inferior contact', and contact 1, labeled 'superior contact') are in the right presumed shell subregion. PA view. **E**. The acute effects of stimulation of each contact on self-reported anxiety and mood in the right NAc. **F** As in **C,** recruitment curves of right NAc-insula fibers derived from patient-specific computational model of axonal activation in response to monopolar stimulation
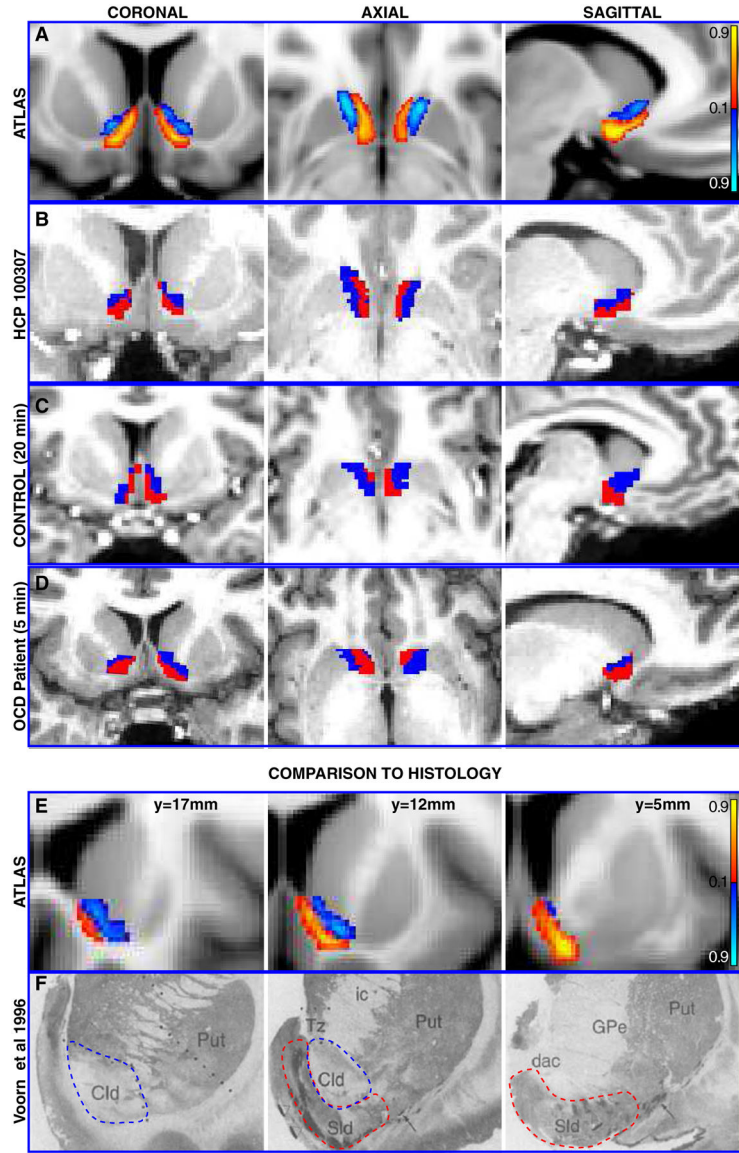
Figure 2. Visualization of cluster output across datasets (A-D) and comparison to histology (EF).
A Coronal, axial, and sagittal views of the probabilistic atlas created from registering all HCP subjects' cluster output to common space (MNI152). Intensity values indicate strength of evidence for the presence of a given subregion. **B** Coronal, axial, and sagittal views of cluster output for a single subject from the HCP dataset. **C** Coronal, axial, and sagittal views of output from application of clustering procedure to a separate, lower quality dataset with ~20 minute acquisition time. **D** Coronal, axial, and sagittal views of cluster output from a third, clinically-acquired dataset from a human patient with a 5 minute acquisition time. **E** Serial coronal views of left NAc subregions from probabilistic atlas for comparison with **F**, histological sections from human NAc depicting core-like (blue dashed line) and shell-like (red dashed line) divisions of left NAc, adapted with permission from Voorn *et al* (1996).
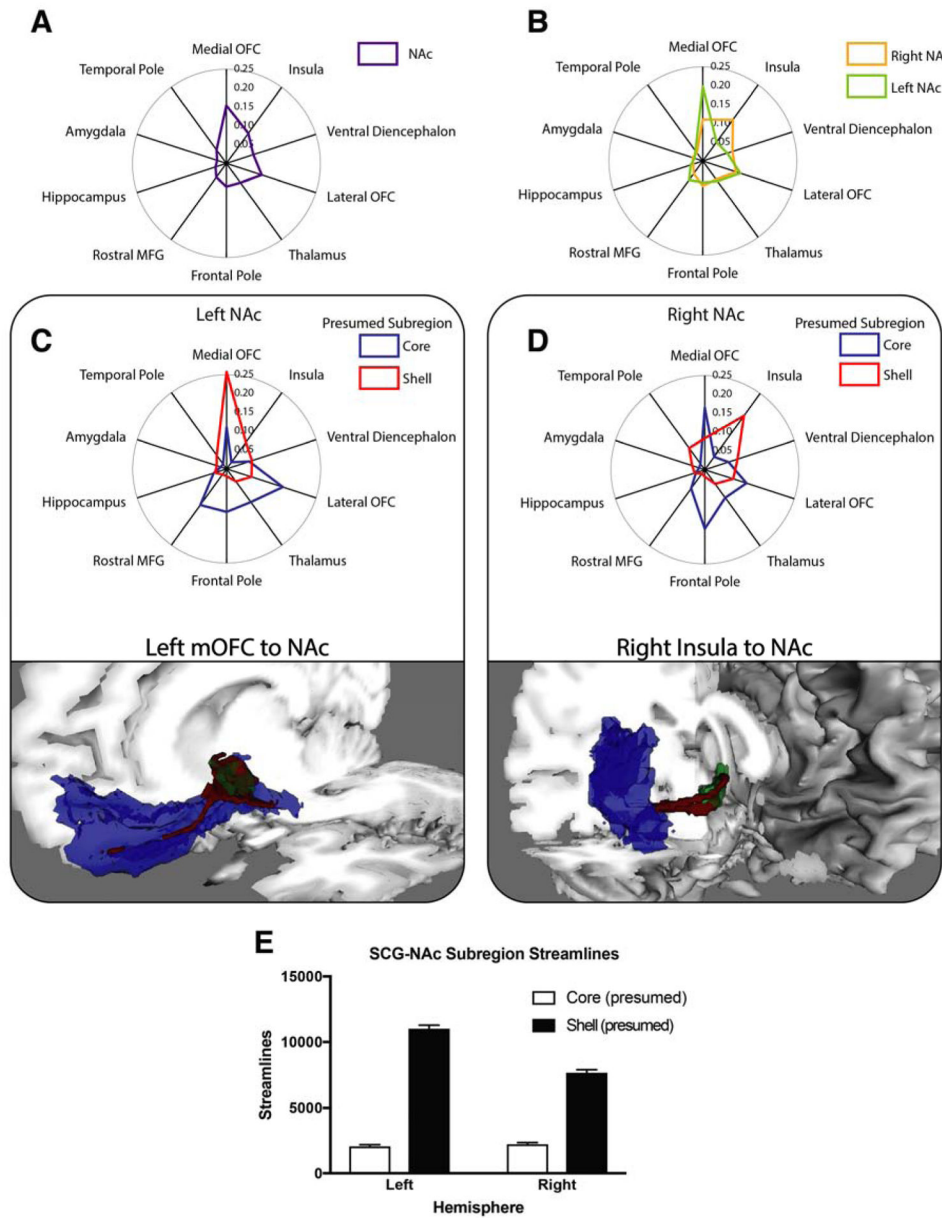
Sld = shell-like division, cld = core-like-division, ic = internal capsule, Tz = transitional zone, Put = Putamen, GPe = Globus Pallidus external division, dac = dorsal anterior commissure terminology taken from Voorn *et al*

Figure 3. Connectivity of the NAc and connectivity-defined subregions.
A,B Distance along each spoke of radial plots indicates proportion of streamlines intersecting that region of interest. **A** Streamline proportions of whole NAc averaged across hemispheres demonstrates mOFC has most robust connectivity to NAc. **B** Streamline probability of whole NAc separated by hemisphere. **C,D** (top) Connectivity profiles of tractography-defined shell (red) and core (blue) subregions of left (**C**) and right (**D**) NAc paired with visualization of principal tracts. **C** (bottom) Oblique view of tract (red) connecting the mOFC (blue) with the left NAc (green). **D** (bottom) View of tract (red) connecting the insula (blue) with the right NAc (green). Tract visualizations created by thresholding the probabilistic streamline map at 25% of the peak value. **E** Comparison of the number of streamlines intersecting tractography-defined presumed shell and core subregions
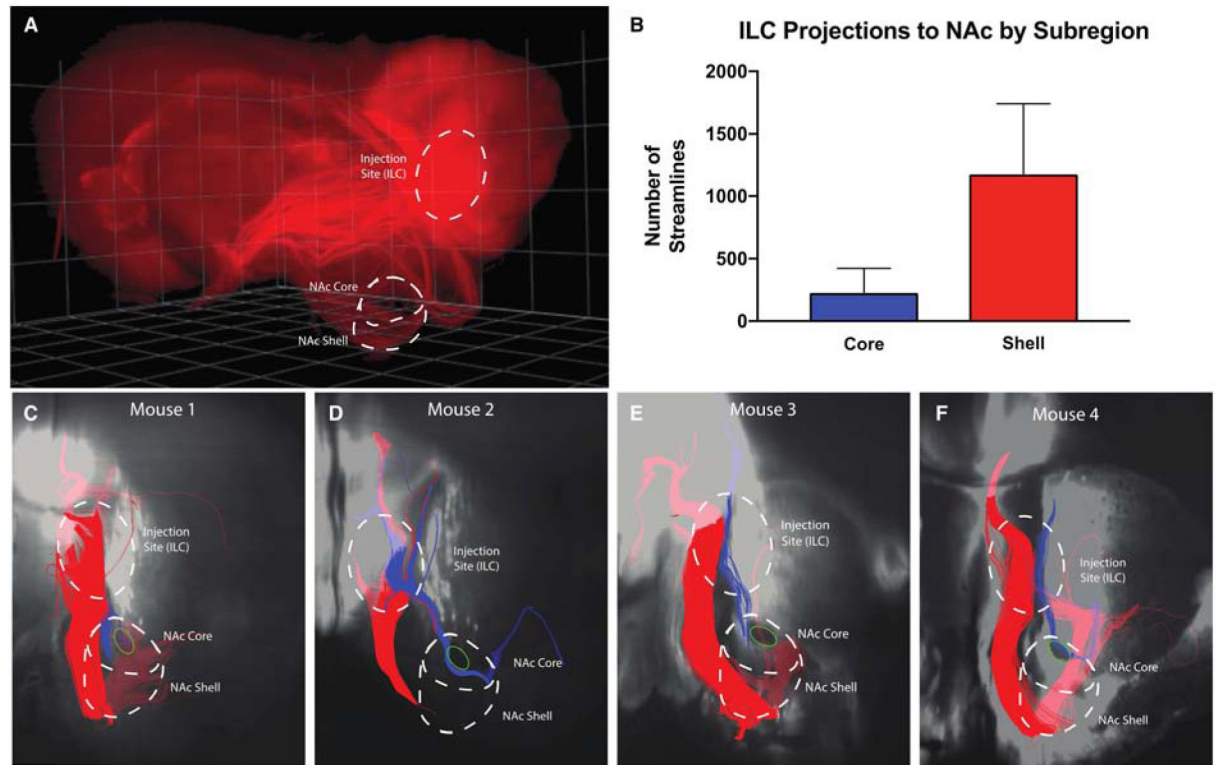
from SCG. NAc, nucleus accumbens, mOFC, medial orbitofrontal cortex, SCG, subcallosal gyrus.

Author Manuscript

Author Manuscript

Author Manuscript

Author Manuscript

Figure 4. CLARITY Tractography demonstrates separate tracts connecting murine infralimbic cortex (ILC) and NAc core and shell.
A Raw oblique three-dimensional CLARITY image showing virally-induced florescence of projections from ILC. Borders of ILC, NAc core and shell outlined in white. **B** Comparison of the mean number of streamlines in each tract averaged across mice. **C** Tractography results with a representative coronal slice from a mouse brain. Both tracts emanate from injection site in ILC and descend toward the NAc. The larger tract (red) projects through the NAc shell subregion, while the other tract (blue) passes immediately adjacent to the anterior commissure (green oval) in the NAc core. **D-F** Tractography results from 3 additional mice. As in **C**, injection sites and NAc subregions are outlined and ensembles projecting to core and shell are colored blue and red, respectively.
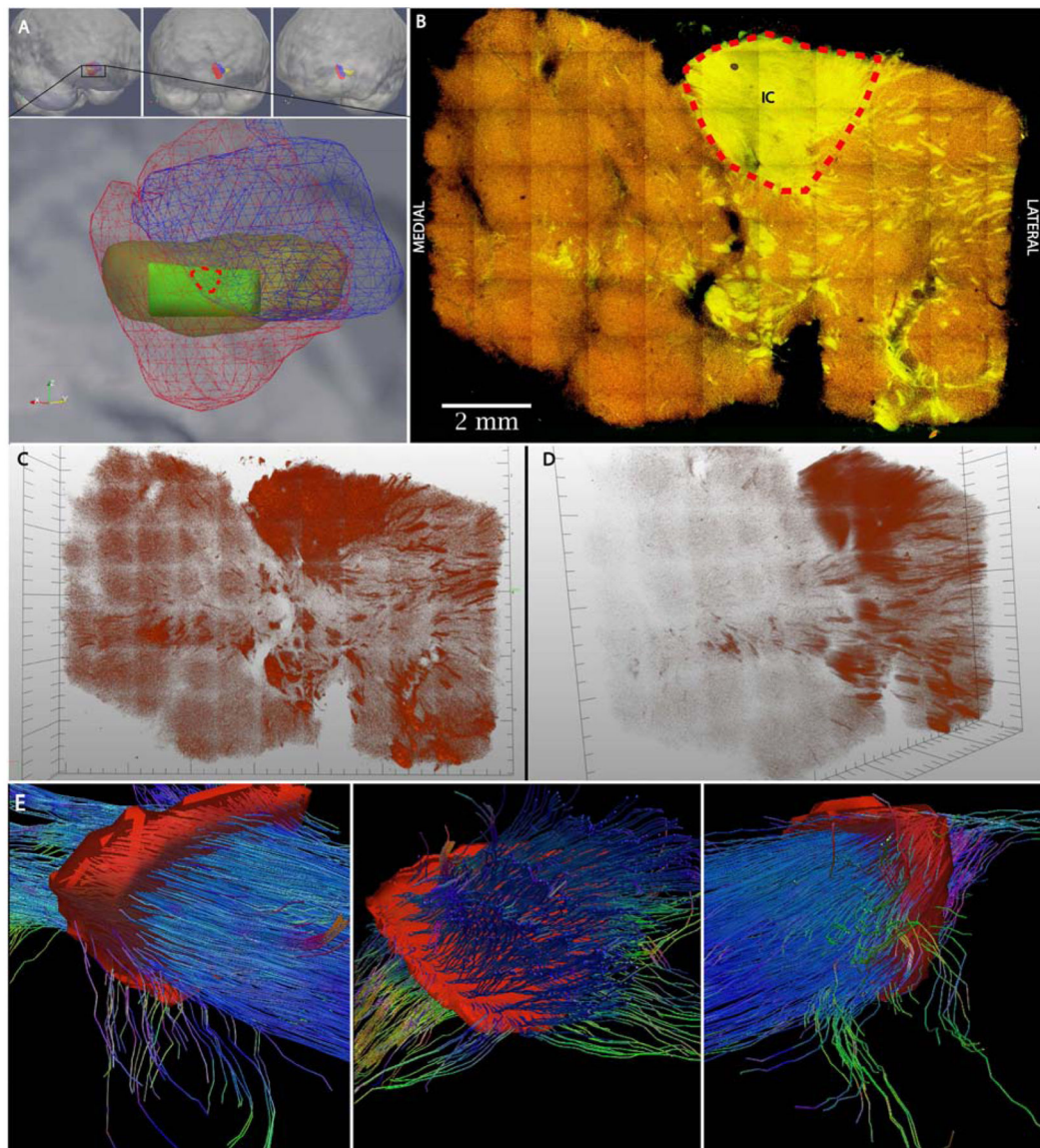
Figure 5. CLARITY and tractography of human post-mortem sample visualize fibers during passage to and from the ventral internal capsule.

A Top: Medial oblique (left), frontal (center), and lateral oblique (right) views of volume rendering post-mortem tissue sample (yellow) merged to probabilistic atlas NAc subregions (core-blue, shell-red). Bottom panel: Close-up medial oblique view showing NAc subregions (core-blue wireframe, shell-red wireframe) and post-mortem tissue sample (yellow) with volume of clarified tissue (green) from shell. Red dotted line indicates contour of seed mask used for tractography in panel **E. B** Maximum intensity projection of clarified human tissue. Nerve fibers can be seen transiting to and from the ventral internal capsule as a result of their strong autofluorescence (yellow) against the weakly calbindin-staining shell (red). Red dotted line indicates contour of ventral internal capsule used as seed mask used for tractography in panels **E. C,D** Frontal and medial oblique volumetric views of autofluorescence channel of clarified human NAc sample (see Video 1 for further perspectives). **E** Medial oblique (left), frontal (center), and lateral oblique (right) views of

tractography results from 7T acquisition of post-mortem sample. Seed mask indicated in red and depth represents approximate thickness of clarified sample. In addition to robust bundle of fibers from internal capsule, vertically and horizontally oriented fibers are visualized on either side. IC = Internal Capsule.

Table 1.

Summary of all MRI Data. All HCP data were acquired on a customized 3T Siemens Skyra capable of achieving 100 mT/m gradients using a 32-channel head coil.

		HCP Data		Standard Data		Patient Data		Postmortem Data	
Data Type	Diffusion	Functional (Gambling Task)	Structural (T1w)	Diffusion	Structural (T1w)	Diffusion	Structural (T1w)	Diffusion	Structural (T1w)
Sequence	Spin Echo EPI	Gradient Echo EPI	3D MPRAGE	Spin Echo Single Shot EPI	MPRAGE	Spin Echo Single Shot EPI	BRAVO	Spin Echo Single Shot EPI	FLASH 3D
TE / TR (ms)	89.5 / 5520	33.1 / 720	2.14 / 2400 / 1000 (TI)	74 / 8397	2.3 / 2530 / 1100 (TI)	72.1 / 13000	3.724 / 9.472 / 400 (TI)	27.4 / 500	20 / 58.6 / 20 (TI)
Flip Angle (o)	78	52	8	90	7	90	13	90	22
Field-of-View (mm2)	210×180	208×180	224×224	220×220	200×200	256×256	256×256	11 × 30	11 × 30
Matrix Size	168×144	104×90	320×320	110×110	200×200	96×96	256×256	55 × 150	110 × 300
In-plane Res. (mm2)	1.25×1.25	2×2	0.7×0.7	2×2	1×1	2.7×2.7	1×1	0.2×0.2	0.1×0.1
Slice Thick. (mm)	1.25	2	0.7	2	1	2.5	1	0.2	0.1
Number of Slices	111 Axial	72 Axial	256 Sagittal	66 Axial	176 Sagittal	69 Axial	176 Axial	60 Axial	120 Axial
Runs	6	2	2	1	1	1	1	6	1
Acq. Time (min)	9:50 (59 total)	3:12 (6:24 total)	7:40 (15:20 total)	20:58	7:25	6:43	4:00	1:00:00 (6hrs total)	13:58
Diffusion Encoding (s/mm2)	6×b=0 90 dir. × b=1,000, 2,000, 3000	\	\	10×b=0 60 dir. × b=1000, 80 dir. × b=2500	\	1 ×b=0 30 dir. × b=1000	\	6 ×b=0 125 dir × b=1000, 2000; 250 dir × b=4000,8000	\